Vietnam Journal of Science and Technology ***61*** *(5) (2023) 819-829*

doi:10.15625/2525-2518/16900

Controlling near-field coupling for switchable metamaterial between absorption and polarization-conversion functions

Nguyen Van Ngoc[1, 2, †], Le Van Long[1, †], Dinh Ngoc Dzung[1], Tran Van Huynh[1, 3], Nguyen Thi Mai[2], Bui Son Tung[1, 2, *], Bui Xuan Khuyen[1, 2, *], Vu Dinh Lam[1]

[1]*Graduate University of Science and Technology, Vietnam Academy of Science and Technology, 18 Hoang Quoc Viet, Cau Giay, Ha Noi, Viet Nam*

[2]*Institute of Materials Science, Vietnam Academy of Science and Technology, 18 Hoang Quoc Viet, Cau Giay, Ha Noi, Viet Nam*

[3]*University of Fire Prevention and Fighting, Ha Noi, Viet Nam*

[*]Emails: *tungbs@ims.vast.ac.vn, khuyenbx@ims.vast.ac.vn*

†*These authors have the same contribution*

Received 27 January 2022; Accepted for publication: 8 June 2023

Abstract. In this paper, a multifunctional metamaterial (MM) structure capable of performing as a polarization converter and absorber is proposed. By using DC bias voltage to control the capacitor of the integrated varactor, the near-field coupling in our structure can be manipulated to flexibly switch between polarization conversion (PC) mode and perfect absorption (PA) mode. The numerical simulation results show that in PC mode the polarization conversion ratio exceeds 90 % at 4 GHz, while the dual-band absorption is observed in PA mode with a value close to 90 % at 3.5 and 5.5 GHz. In addition, we also reduce the geometric sizes of the proposed structure to further examine its performance in the THz frequency range. Owing to its excellent characteristics in both PA and PC modes, the proposed hybrid MM structure is promising to apply in many fields such as radar, remote sensing, and satellite.

Keywords: Metamaterials, polarization conversion, perfect absorption.

Classification numbers: 2.1.2, 2.2.2, 2.10.1.

1. INTRODUCTION

The emergence of metamaterial (MM) has opened-up new directions for the field of materials science. MMs are composed of artificial atoms, which allows them to possess many extraordinary properties such as negative refractive index [1], perfect absorption (PA) [2], and polarization conversion (PC) [3]. In 2008, the first metamaterial perfect absorption (MPA) was experimentally devised by Landy *et al.* [4]. Inspired by the work of Landy, many single-/multi-/broadband MPAs which operate in a frequency range from radio to visible region have been proposed [5, 6]. With potential applications on practical devices such as sensors [7], solar cells

[8], and thermal imaging in the military field [9], it is not surprising that MPA has still received a lot of attention over the past decade. Besides, the polarization of electromagnetic (EM) wave is also a property of interest due to its application in many areas such as antennas, navigation space, and communications information [10 - 12]. Even though certain types of natural materials can efficiently manipulate the polarization properties of electromagnetic waves, the bulky size limits their potential to be integrated into compact electronic devices. Therefore, with the advantage of the miniature structure and the ability to be operated in a wide range of frequencies, MM is able to replace natural materials for different purposes, such as dual-polarized radars, polarimetry measurements, fiberoptic transportations, and MIMO (multi-input/multioutput) communications [13, 14].

So far, various types of PC and PA using MM have been intensively studied in the microwave, GHz, THz, and optical frequency bands [15 - 18]. However, these studies have mainly focused on structures which only operate in PA or PC mode, but not both. Although multifunctional materials that flexibly switch between two modes have great potential, they have not received sufficient attention. Therefore, in this paper, we present a method to control near-field coupling in a hybrid GHz metamaterial structure by integrating varactor diode, which is capable of flexibly switching between PC and PA functions in the same frequency region. By manipulating the capacitance of the diode, the MM configuration can be simply transformed between the 1st basic structure, which is symmetric, and the 2nd basic structure, which is asymmetric. Consequently, the near-field coupling in MM can be inactive or active, creating the PA or PC functions, respectively.

2. DESIGN AND SIMULATION

The proposed MM structure with its parameters is shown in Figure 1. The structure consists of three layers. In detail, two copper layers are on the top and bottom with a conductivity of 5.8 x 10^7 S/m. The back copper plate is continuous to prevent the transmission of the EM waves while the other one located at the front is patterned. These two layers are separated by the dielectric layer with a thickness of *t*. Rogers RO3003 with the relative permittivity of 3 and its loss tangent of 0.001 is chosen as the material of this dielectric layer. In order to switch between PA and PC modes by applying the external voltage, we integrate a varactor diode in the right air gap of the patterned copper outer square as shown in Figure 1.

Table 1. Effective circuit parameters for varactor diode SMV2019-079LF.

VR (V)	C (pF)	R (Ω)	L (nH)
0	2.31	4.51	0.7
-4	0.84	4.04	0.7
-7	0.55	3.66	0.7
-11	0.38	3.18	0.7
-14	0.31	2.86	0.7
-16	0.27	2.65	0.7
-19	0.24	2.38	0,7

With the advantage that the capacitance can be changed by applying a DC bias voltage, varactor diodes are preferred for using in an MM structure capable of switching between PA and PC modes. In this study, we choose the SMV2019-079LF varactor diode manufactured by Skywork. Its capacitance varies from 2.31 to 0.24 pF because the DC reverse bias voltage applied over the feeding lines will vary from 0 to 19 V [19]. The effective values (R, L, and C) are shown in Table 1.

Our simulation uses CST Microwave Studio software [20] with a chosen frequency range from 2 to 7 GHz. In this study, the electric field vector of the incident EM wave oriented along the *u* axis is inclined at an angle of 45° to the *y* axis as shown in Fig. 1. The reflection matrix (*R*) is described as follows [21]:

$$R = \begin{pmatrix} R_{vv} & R_{vu} \\ R_{uv} & R_{uu} \end{pmatrix} \tag{1}$$

here, the incident EM wave is in the *u*-polarized state, so only the two important quantities need to be considered: the co-polarized reflection coefficient (R_{uu}) and the cross-polarized one (R_{vu}). Since the copper plane is continuous at the bottom, there is no transmitted wave in this structure. Therefore, absorption is defined as:

$$A = 1 - |R_{uu}|^2 - |R_{vu}|^2 \tag{2}$$

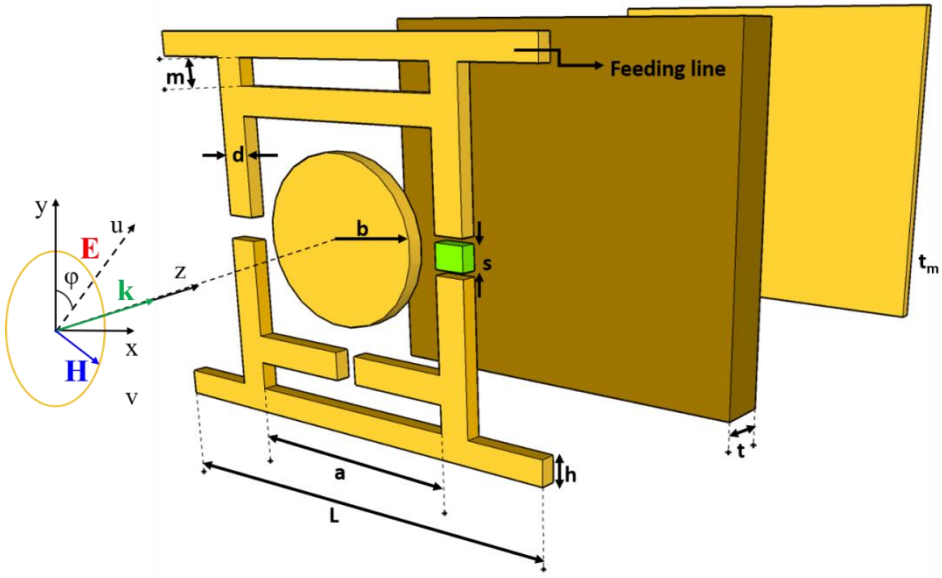

Figure 1. Three-dimensional design of the proposed unit cell with optimized parameters L = 24.5, a = 22, b = 11, s = 1.2, d = 4, m = 0.5, h = 0.5, t = 2, and t_m = 0.035 mm.

This calculation includes both R_{uu} and R_{vu} because the reflected wave exhibits both *u*- and *v*-polarized waves. Besides, the polarization conversion ratio (PCR) can be expressed as [21]:

$$PCR = \frac{|R_{vu}|^2}{|R_{uu}|^2 + |R_{vu}|^2} \tag{3}$$

3. RESULTS AND DISCUSSION

Figure 2(a) depicts the reflection coefficients of the MM structure when the voltage is 0 V. Owing to equation (2), the absorption is calculated and shown in Figure 2(b). Two absorption

peaks are observed at 3.5 and 5.5 GHz with the absorption values of 90.3% and 89.6%, respectively. This result shows that when the bias voltage is 0 V, the MM structure operates in PA mode. To clarify the role of varactor in our structure, we also examined the structure without varactor, which we call "the first basic structure". Besides the lack of varactor, this 1st basic structure has only two gaps compared to our proposed structure as shown in the inset of Figure 2(c). In Figure 2(c-d), it is clear that the 1st basic structure with 2 gaps also gives results equivalent to our proposed MM structure with varactor diode when the external voltage is 0 V. The shift of the absorption frequency between structures with and without diode can be explained by the difference between the metal continuous wire and the integrated capacitor of zero voltage. Theoretically, the EM properties of the MM (with the zero voltage) are similar to those of the 1st basic MM (with the metal continuous wire). Current can flow through two parts of the metal wire like the case of the continuous wire. However, the MM structure using diode will not be exactly the same as the 1st basic structure due to the presence of the gap. Hence, the total inductance will be different, causing the resonance frequency to also be different.

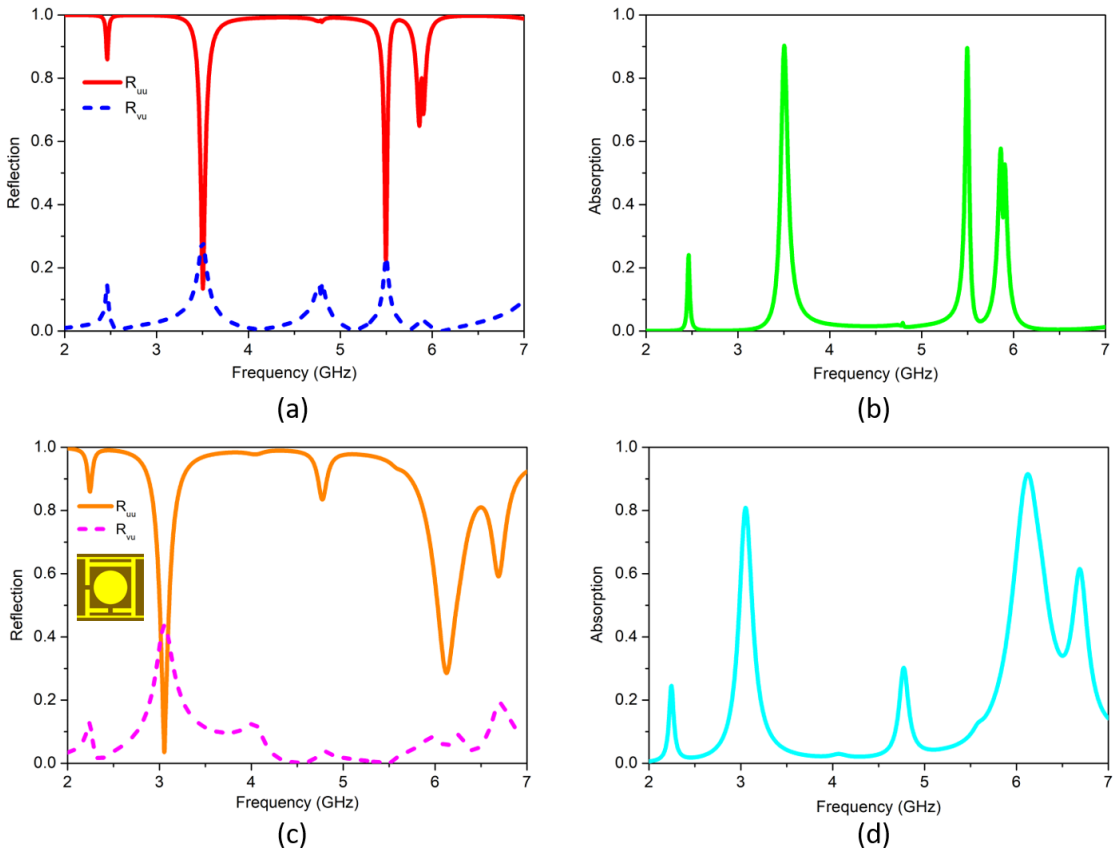

Figure 2. In the PA mode, the simulated results of (a) co- and cross-polarized reflection coefficients and of (b) absorption for the hybrid MM at a bias voltage of 0 V, and (c) and (d), respectively, for the first basic structure MM including a meta-surface with only two air gaps.

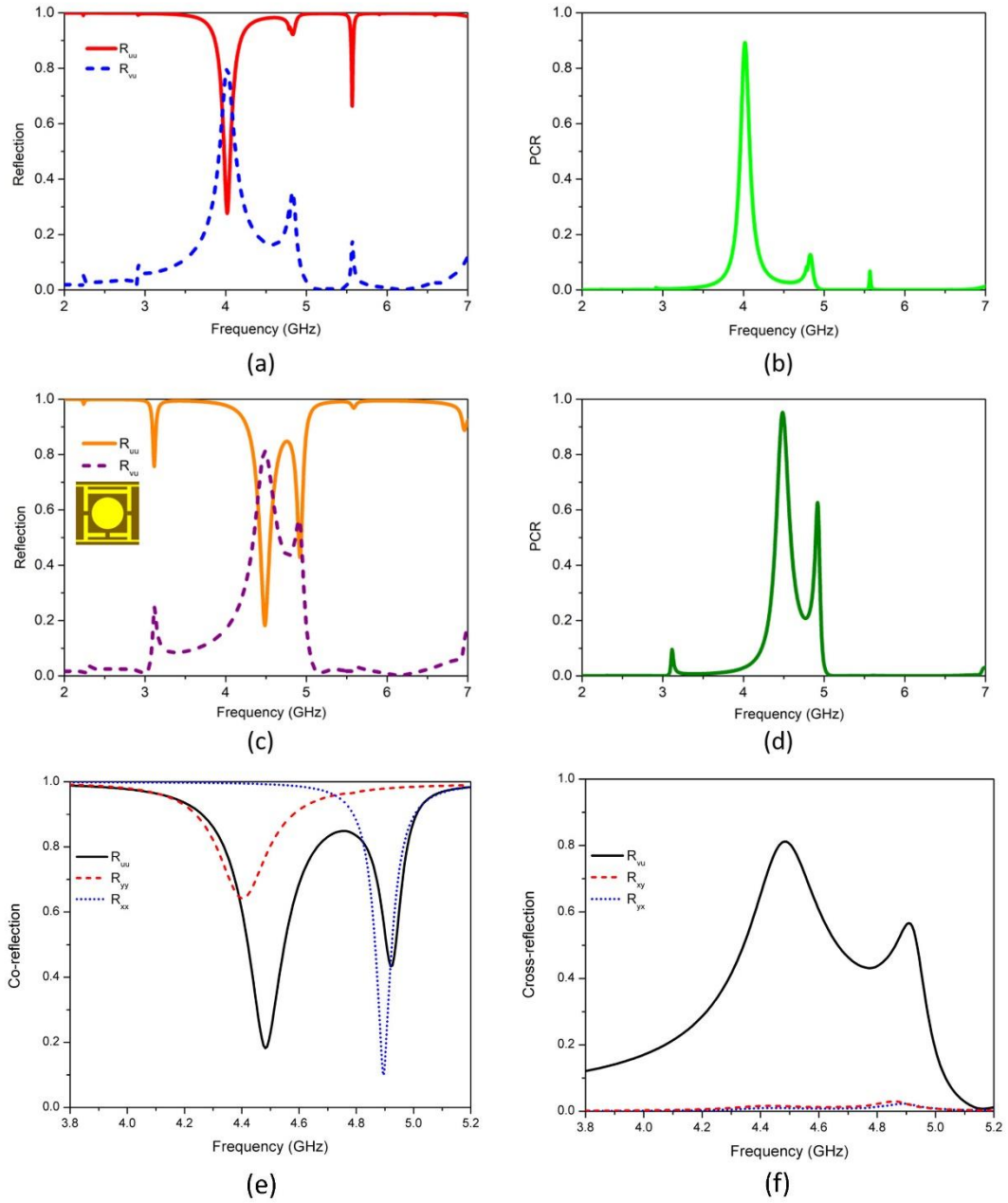

Figure 3. In the PC case, (a) simulated reflection coefficients R_{vu} and R_{uu}, and (b) PCR for the hybrid MM at a reverse bias voltage of −19 V. Simulated (c) R_{vu}, R_{uu}, and (d) PCR for the second basic MM with three air gaps on the meta-surface. (e) Co- and (f) cross-reflection spectra of MM (*u*-polarization) and MM in decoupled modes (*y*- and *x*-polarizations).

When the applied voltage is -19V, the capacitance of the varactor diode decreases to 0.24 pF. Consequently, our proposed MM structure changes from absorption mode to PC mode as shown in Figure 3(a-b). Figure 3(a) shows that at 4 GHz, the co-polarized reflection coefficient R_{uu} is lower than 0.3 while the cross-polarized reflectance coefficient R_{vu} is up to 0.8. From equation (3), the PCR is calculated and shown in Fig. 3(b). It is easy to observe that at 4 GHz

PCR reaches approximately 90 %. The high value of PCR demonstrates the excellent polarization conversion efficiency of our structure. Fig. 3(c-d) shows the simulation results of "the 2nd basic MM structure" which has 3 gaps without integrated diodes (inset of Figure 3(c)). It should be mentioned that, to achieve PC mode, the structure needs to be asymmetric. Therefore, an extra gap is created on the right side of the outer square (at the diode integration site), that breaks the symmetry of the MM structure. These results are quite similar to the results of our proposed MM structure when the external voltage is -19V. Therefore, the simulation results of the 1st and 2nd basic structures indicate that the variation of the diode capacitor under the applied voltage leads to the shift of our structure from the 1st to 2nd basic structures. This means that the conversion between PC and PA is achieved by exploiting varactor diode.

It is noteworthy that the electric field of incoming wave is polarized in the *u*-direction, which can be decomposed to the sub-components in the *y*- and *x*-directions. Figure 3(e-f) presents the co- and cross-reflection spectra of the 2nd basic MM (*u*-polarization) and 2nd basic MM in decoupled modes (*y*- and *x*-polarizations) around the high-PCR region. Because the presence of the additional gap makes the 2nd basic MM structure asymmetric, the near-field effect can be created in this condition. It can be observed that two resonances are excited at 4.4 and 4.9 GHz in the *y*- and *x*-polarizations, respectively. The near-field coupling of the decoupled resonances creates the reflection spectrum of MM with a reflection peak lying between two resonance dips. It should be mentioned that because the decoupled resonance modes are corresponding to two orthogonal polarizations, their near-field coupling gives rise to a PC phenomenon with much higher cross-reflection than the decoupled mode alone.

The dependence of the reflection coefficient and PCR on voltage is also clarified by simulations. The results in Figure 4 indicate that when the voltage drops from 0 V to -19 V, the PCR tends to increase and reaches 90 % at -19V. This trend further emphasizes the importance of diode capacitance in switching the state of the proposed MM structure.

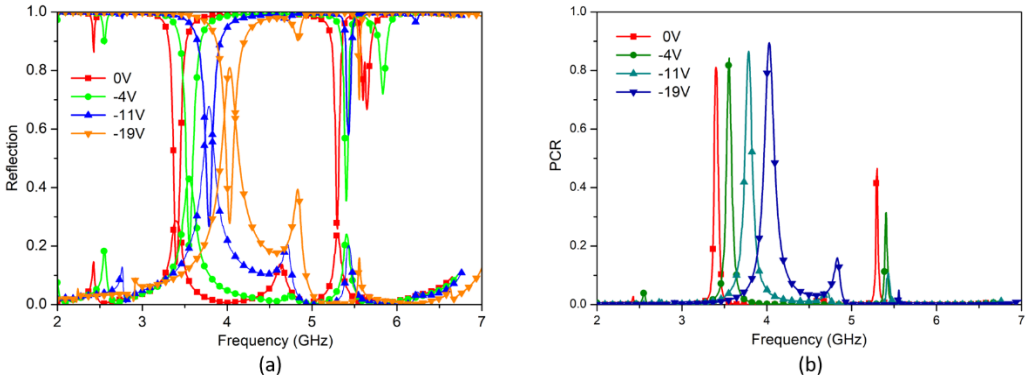

Figure 4. Simulated dependence of (a) the co-polarized reflection coefficient R_{uu} and cross-polarized one R_{vu}, and (b) the corresponding PCR of the hybrid MM, upon bias voltage varied from 0 to −19 V.

To explain the polarization conversion mechanism, we analyze the incident electromagnetic wave E_i as shown in Fig. 4(a), where E_i is oriented along the *u* axis and decomposed into *x* and *y* components according to formula [4]:

$$E_i = \hat{x}E_{ix}e^{i\varphi} + \hat{y}E_{iy}e^{i\varphi} \quad (4)$$

After impinging on the MM structure, the electromagnetic wave is reflected and has the following expression:

$$E_r = \hat{x}E_{rx} + \hat{y}E_{ry} \tag{5}$$

$$= \hat{x}\left(R_{xx}E_{ix}e^{i\varphi_{xx}} + R_{xy}E_{iy}e^{i\varphi_{xy}}\right)$$

$$+ \hat{y}\left(R_{yy}E_{iy}e^{i\varphi_{yy}} + R_{yx}E_{ix}e^{i\varphi_{yx}}\right),$$

where $\hat{x}$ and $\hat{y}$ are the unit vectors, (R_{xx}, R_{yy}) and (R_{xy}, R_{yx}) are the magnitudes of the co- and cross-reflection in the *x* and *y* axes with the respective phases (φ_{xx}, φ_{yy}) and (φ_{xy}, φ_{yx}). Because the proposed MM structure is capable of switching polarization, in the expression of *Er*, we must take into account both co- and cross-polarized reflection coefficients.

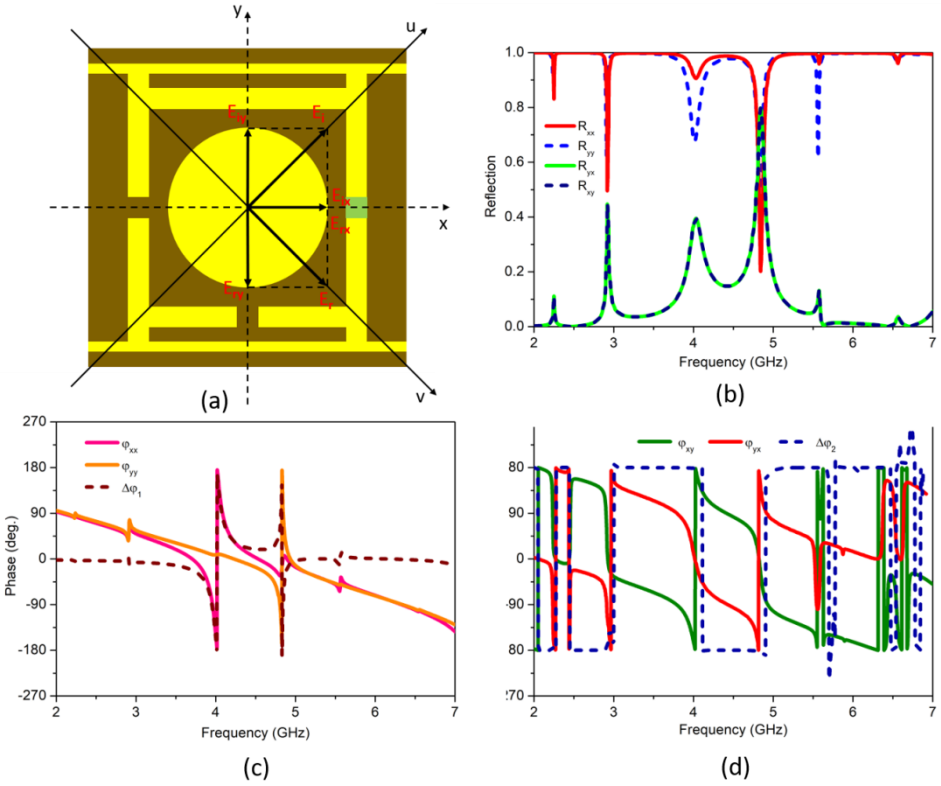

Figure 5. (a) Intuitive scheme of *y*- to *x*-polarization conversion. (b) Magnitude of the *u*- and *v*-reflection coefficients. The reflected phases of (c) co- and (d) cross-polarized reflection coefficients when the electric vector of incident EM wave is along *u*- and *v*-axis.

Further simulations of the magnitude and phase of the reflectance coefficients along the *x* and *y* axes are presented in Figure 5(b-d). The magnitude of the reflection coefficients is shown in Figure 5(c). It can be seen that R_{xy} and R_{yx} are completely similar. The other two coefficients, R_{xx} and R_{yy}, are not significantly different. At 4 GHz, the phase retardation between the co- and cross-reflection coefficients is 180°. This result can be observed in Fig. 4(c-d) where $\Delta\varphi_1 = \varphi_{xx} - \varphi_{yy}$ is the phase difference between the co-reflection coefficients and $\Delta\varphi_2 = \varphi_{xy} - \varphi_{yx}$ is the phase difference of the cross-reflection coefficients. According to equation (5), this out-of-phase induces perpendicularity in the orientation of the incident and reflected waves. It means our MM structure under the applied voltage of -19V is capable of rotating the polarization plane with an angle of 90°.

To provide more details on the mechanism of PA and PC modes, we also investigate the surface-induced current distribution at the resonant frequency, as shown in Figure 6. The results in Figure 6(a-b) show that at both frequencies the antiparallel current between the top and bottom metal layers exhibit magnetic resonance. In addition, the simulation results shown in Figure 6(c) in PC mode at 4 GHz are accumulated in the top right corner and bottom left corner of the outer square. As mentioned, Figure 6(c) also shows that the currents at the top and bottom are antiparallel so it can be concluded that the PC mode gives similar results for magnetic resonance.

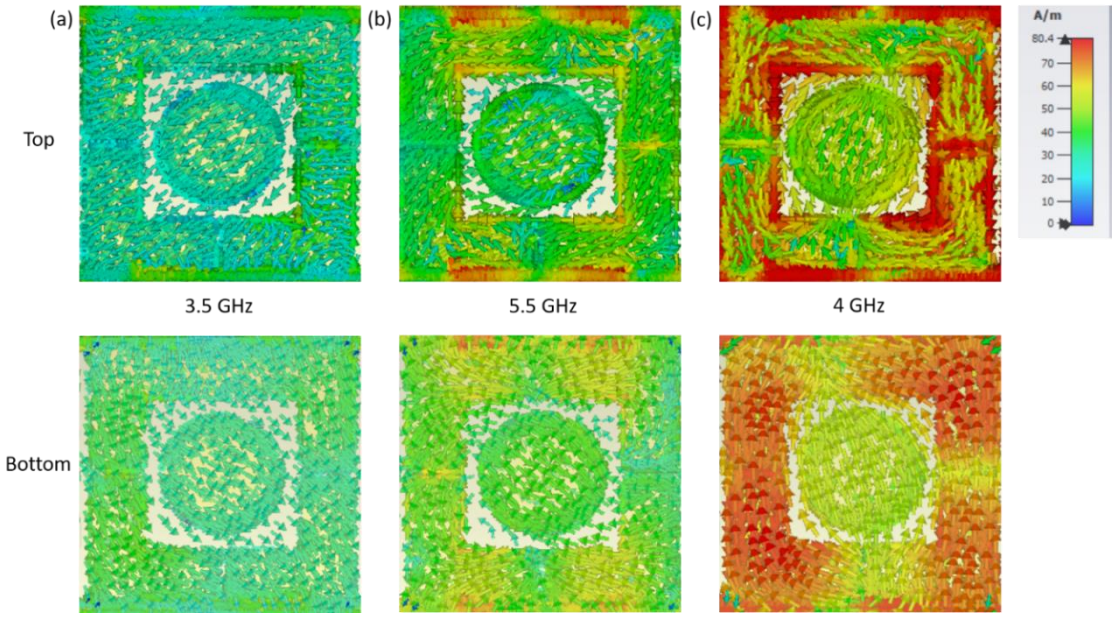

Figure 6. Distribution of surface induced currents in the top and bottom layers at resonant frequencies of (a) 3.5, (b) 5.5 in the case of the PA mode (no bias voltage), and (c) 4.0 GHz for the PC mode (at a bias voltage of −19 V).

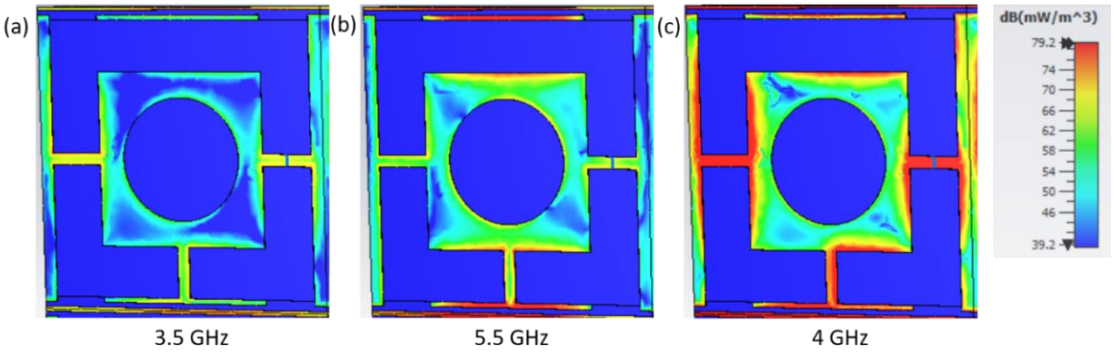

Figure 7. Distribution of the power-loss density at (a) 3.5, (b) 5.5 in the PA mode (no bias voltage), and (c) 4.0 GHz for the PC mode (at a bias voltage of −19 V).

The power-loss density distribution of the structure is shown in Figure 7. It can be easily seen that at all three resonant frequencies, the losses are concentrated at the position with strong induced current. The power loss at 3.5 GHz is concentrated only around three gaps of the square (at a high accumulation of the surface induced current). In contrast, the power loss is

concentrated around the space between the square with the inner circle and the feeding line at 5.5 GHz. Furthermore, at a resonant frequency (4 GHz) for the PC mode, the results in Fig. 7(c) indicate that the power loss is mainly concentrated in the 3 gaps which play an important role in inducing a high PCR because of the great anisotropic feature.

Finally, we examine the performance of the 1st and 2nd basic structures in the THz frequency region by reducing their structure parameters. For these reasons, silver (conductivity σ = 6.3×10^7 S/m) is chosen to replace copper for the top and bottom metal layers, while Si (permittivity 11.9) is used as a dielectric layer instead of Rogers. The optimized geometry parameters are L = 24.5; a = 22; b = 11; s = 1.2; d = 4; m = 0.5; h = 0.5; t = 2 and t_m = 0.035 μm. The corresponding co- and cross-polarized reflections of both structures at THz frequency range are presented in Figure 8. In Figure 8(a), the 1st basic MM structure plays the role of PA with absorption peaks at 2.29 THz (82.3%) and 3.6 THz (99.5%), where R_{uu} = 0.26 and 0.07 and R_{vu} = 0.35 and 0.07, respectively. In Figure 8(b), the 2nd basic structure gives co- and cross-polarized reflection coefficients of 0.3 and 0.67 at 2.6 THz, respectively. The corresponding PCR coefficient is quite high (83 %) at this resonance frequency, indicating that the 2nd basic structure activated a function similar to the PC mode in the THz frequency band. The above results suggest that the MM structure capable of PA/PC conversion in the THz frequency region can be designed by reducing the structure parameters of the aforementioned structure in the GHz region. It is noteworthy that different materials such as liquid crystal [22] and varactor diodes based on metal-semiconductor-metal 2-dimensional electron gas [23] can be used to replace varactor diode and are feasible to be employed for the THz fabrication. This research direction promises to create MMs capable of absorption/PC conversion for application in smart devices and components in the THz frequency region.

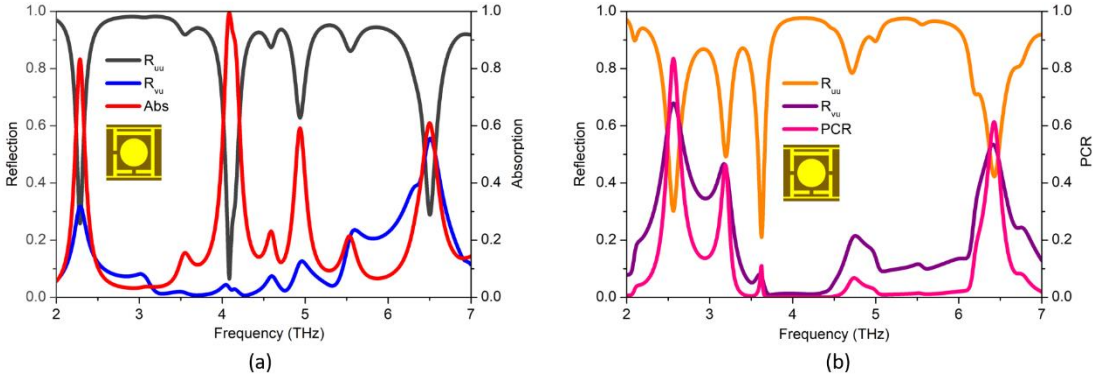

Figure 8. Further investigation in the THz range for (a) the PA mode by using the downsized first basic MM, and (b) the PC one by exploiting the downsized second basic MM.

4. CONCLUSIONS

We have proposed a switchable PA/PC function based on MM in GHz region. By taking advantage of a varactor diode whose capacitance can be efficiently controlled by the bias voltage, the near-field coupling of MM can be controlled, leading to the transformation of dual-band absorption and cross-polarization conversion states. The role of varactor diode (applied bias voltage varies from 0 to -19 V) is clarified through the 1st and 2nd basic structures to achieve dual functionality for both PA and PC by using only one hybrid MM structure. The switching

mechanism has also been elucidated through the investigation of surface current density distribution and power loss. The agreement between simulation and experiment indicates that the proposed structure is promising for the development of a future generation of advanced devices that work in EM detection, stealth technology, communication systems, and so on. Furthermore, the metamaterial basic structure is also scaled down and simulated in the THz region, which shows good performances of PA and PC functions, too. Therefore, a THz switchable PA/PC function based on metamaterial is possible to be realized and to be applied in THz technology by simply replacing varactor diode with metal-dielectric transition materials.

Acknowledgements. This research was funded by the Vietnam National Foundation for Science and Technology Development (NAFOSTED) grant number 103.99-2019.31 and funded by the Graduate University of Science and Technology under grant number GUST.STS.ĐT2019-KHVL01.

CRediT authorship contribution statement. Nguyen Van Ngoc: Simulations and paper writing, Le Van Long: Simulations and formal analysis, Dinh Ngoc Dzung: Parametric analysis, Tran Van Huynh: Formal analysis, Nguyen Thi Mai: Formal analysis, Bui Son Tung: Conceptualization, Bui Xuan Khuyen: Methodology, Vu Dinh Lam: Supervision.

Declaration of competing interest. The authors declare that they have no known competing financial interests or personal relationships that could have appeared to influence the work reported in this paper.

REFERENCES

1. Shalaev V. M. - Optical negative-index metamaterials, Nat. Phot. **1** (1) (2007) 41-48. https://doi.org/10.1038/nphoton.2006.49.
2. Li W. and Valentine J. - Metamaterial perfect absorber based hot electron photodetection, Nano Lett. **14** (6) (2014) 3510-3514. https://doi.org/10.1021/nl501090w.
3. Khan M. I., Fraz Q. and Tahir F. A. - Ultra-wideband cross polarization conversion metasurface insensitive to incidence angle, J. Appl. Phys. **121** (4) (2017) 045103. https://doi.org/10.1063/1.4974849.
4. Landy N. I., Sajuyigbe S., Mock J. J., Smith D. R. and Padilla W. J. - Perfect metamaterial absorber, Phys. Rev. Lett. **100** (20) (2008) 207402. https://doi.org/10.1103/PhysRevLett.100.207402.
5. Kim Y. J., Hwang J. S., Yoo Y. J., Khuyen B. X., Rhee J. Y., Chen X. and Lee Y. - Ultrathin microwave metamaterial absorber utilizing embedded resistors, J. Phys. D: Appl. Phys. **50** (40) (2017) 405110. https://doi.org/10.1088/1361-6463/aa82f4.
6. Grant J., Ma Y., Saha S., Khalid A. and Cumming D. R. S. - Polarization insensitive, broadband terahertz metamaterial absorber, Opt. Lett. **36** (17) (2011) 3476-3478. https://doi.org/10.1364/OL.36.003476.
7. Prakash D. and Gupta N. - Applications of metamaterial sensors: a review, Int. J. Microw. Wirel. Technol. **14** (1) (2021) 19-33. https://doi.org/10.1017/S1759078721000039.
8. Rufangura P. and Sabah C. - Perfect metamaterial absorber for applications in sustainable and high-efficiency solar cells, J. Nanophotonics. **12** (2) (2018) 026002. https://doi.org/10.1117/1.JNP.12.026002.
9. Watts C. M., Liu X. and Padilla W. J. - Metamaterial electromagnetic wave absorbers, Adv. Mater. **24** (23) (2012) OP98-OP120. https://doi.org/10.1002/adma.201200674.

10. Rahman S. U., Cao Q., Akram M. R., Amin F. and Wang Y. - Multifunctional polarization converting metasurface and its application to reduce the radar cross-section of an isolated MIMO antenna, J. Phys. D: Appl. Phys. **53** (30) (2020) 305001. https://doi.org/10.1088/1361-6463/ab85e7.
11. Dietlein C., Luukanen A., Popovi Z. and Grossman E. - A W-band polarization converter and isolator, IEEE Trans. Antennas Propag. **55** (6) (2007) 1804-1809. http://dx.doi.org/10.1109/TAP.2007.898595.
12. Ren Z., Sun Y., Zhang S., Zhang K., Lin Z. and Wang S. - Wide wavelength range tunable guided-mode resonance filters based on incident angle rotation for all telecommunication bands, Infrared Phys. Technol. **93** (2018) 81-86. https://doi.org/10.1016/j.infrared.2018.07.015.
13. Mookiah P. and Dandekar K. R. - Metamaterial-substrate antenna array for MIMO communication system, IEEE Trans. Antennas Propag. **57** (10) (2009) 3283-3292. https://doi.org/10.1109/TAP.2009.2028638.
14. Glybovski S. B., Tretyakov S. A., Belov P. A., Kivshar Y. S. and Simovski C. R. - Metasurfaces: From microwaves to visible, Phys. Rep. **634** (2016) 1-72. https://doi.org/10.1016/j.physrep.2016.04.004.
15. Khuyen B. X., Tung B. S., Kim Y. J., Hwang J. S., Kim K. W., Rhee J. Y., Lam V. D., Kim Y. H. and Lee Y. P. - Ultra-subwavelength thickness for dual/triple-band metamaterial absorber at very low frequency, Sci. Rep. **8** (2018) 11632. https://doi.org/10.1038/s41598-018-29896-4.
16. Rahmanshahi M., Kourani S. N., Golmohammadi S., Baghban H. and Vahed H. - A tunable perfect THz metamaterial absorber with three absorption peaks based on nonstructured graphene, Plasmonics, **16** (5) (2021) 1665-1676. https://doi.org/10.1007/s11468-021-01432-7.
17. Mostaan S. M. A. and Saghaei H. - A tunable broadband graphene-based metamaterial absorber in the far-infrared region, Opt. Quantum Electron. **53** (2) (2021) 96. https://doi.org/10.1007/s11082-021-02744-y.
18. Bilal R. M. H., Saeed M. A., Choudhury P. K., Baqir M. A., Kamal W., Ali M. M. and Rahim A. A. - Elliptical metallic rings-shaped fractal metamaterial absorber in the visible regime, Sci. Rep. **10** (2020) 14035. https://doi.org/10.1038/s41598-020-71032-8.
19. Zhao J., Cheng Q., Chen J., Qi M. Q., Jiang W. X. and Cui T. J. - A tunable metamaterial absorber using varactor diodes, New J. Phys. **15** (4) (2013) 043049. https://doi.org/10.1088/1367-2630/15/4/043049.
20. https://www.cst.com.
21. Huang X., Chen J. and Yang H. - High-efficiency wideband reflection polarization conversion metasurface for circularly polarized waves, J. Appl. Phys. **122** (4) (2017) 043102. https://doi.org/10.1063/1.4996643.
22. Shrekenhamer D., Chen W-C. and Padilla W. J. - Liquid crystal tunable metamaterial absorber, Phys. Rev. Lett. **110** (17) (2013) 177403. https://doi.org/10.1103/PhysRevLett.110.177403.
23. Nouman M. T., Kim H. W., Woo J. M., Hwang J. H., Kim D., and Jang J. H. - Terahertz modulator based on metamaterials integrated with metal-semiconductor-metal varactors, Sci. Rep. **6** (2016) 26452. https://doi.org/10.1038/srep26452.